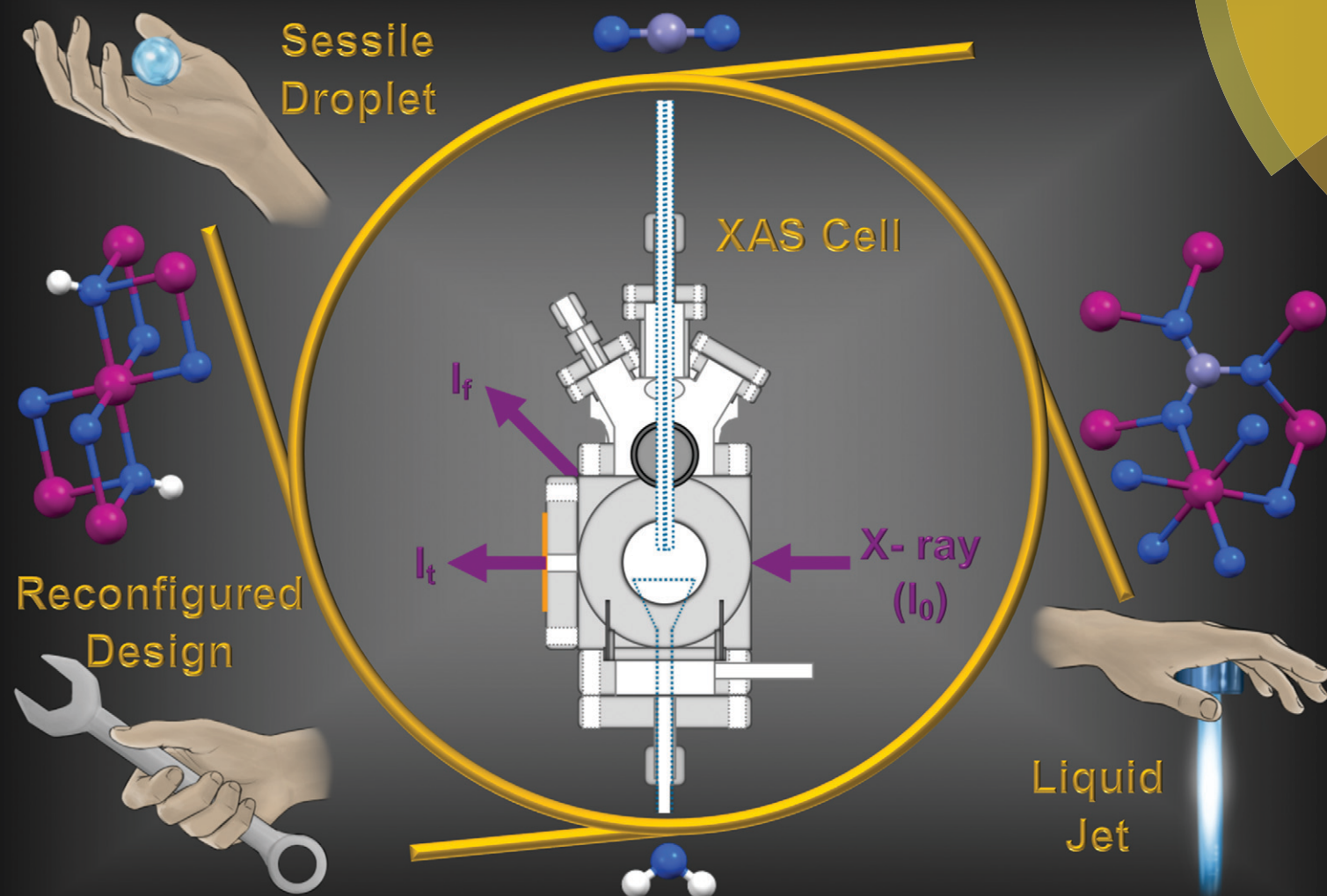


# Reaction Chemistry & Engineering

Linking fundamental chemistry and engineering to create scalable, efficient processes

[rsc.li/reaction-engineering](http://rsc.li/reaction-engineering)



ISSN 2058-9883



ROYAL SOCIETY  
OF CHEMISTRY

Celebrating  
IYPT 2019

## PAPER









S. L. M. Schroeder *et al.*

A versatile liquid-jet/sessile droplet system for *operando* studies of reactions in liquid dispersions and solutions by X-ray absorption spectroscopy



Cite this: *React. Chem. Eng.*, 2019, 4, 679

# A versatile liquid-jet/sessile droplet system for *operando* studies of reactions in liquid dispersions and solutions by X-ray absorption spectroscopy†

S.-Y. Chang, <sup>ac</sup> T. A. Kathyola, <sup>a</sup> E. A. Willneff, <sup>b</sup> Colin John Willis,<sup>d</sup> P. Wilson,<sup>d</sup> P. J. Dowding, <sup>ad</sup> G. Cibi, <sup>c</sup> A. B. Kroner, <sup>c</sup> E. J. Shotton <sup>c</sup> and S. L. M. Schroeder <sup>\*ac</sup>

Herein, we designed a versatile cell for *operando* X-ray absorption spectroscopy (XAS) monitoring of chemical and physical transformations in liquid solutions and dispersions by fluorescence-yield detection. The cell operates under atmospheric pressure, and the composition of the gas phase can be varied, allowing monitoring of gas-liquid reactions. Samples can be examined as a flowing liquid-jet or as a sessile droplet. Both liquid-jet and droplet operations of the cell were demonstrated at the Ca K-edge through time-resolved studies of  $\text{CaCO}_3$  formation from  $\text{CO}_2$  and solid  $\text{Ca(OH)}_2$  in an aqueous suspension. The liquid-jet reaction was performed at 28 °C, and the droplet reaction was performed at ambient temperature, but both configurations had the scope to be modified for operations at higher temperatures. The liquid-jet volumes were recycled, permitting the use of the cell in a continuous sampling loop for process studies in larger reactor vessels. The jet supply tube was interchangeable, permitting adjustment of the jet size through the tubing bore size. Larger bore sizes minimized the pressure drop at the nozzle and thereby the risk of blockage of the liquid supply by the suspended particulates or growth of solid deposits. Sessile droplet operation enabled studies with minimal sample volumes and mechanical disturbances under controlled environmental conditions. The cell is portable and modular and is based on readily available standard vacuum equipment parts. Furthermore, the operation under a He atmosphere allows measurements above 4 keV, covering part of the tender X-ray range, and it is also applicable to the hard X-ray range.

Received 19th September 2018,  
Accepted 6th February 2019

DOI: 10.1039/c8re00207j

rsc.li/reaction-engineering

## 1. Introduction

X-ray absorption spectroscopy (XAS) provides element-specific molecular-level information about the local electronic structure of materials and thus deep insight into their chemical speciation including oxidation states and local coordination geometry. Its sensitivity to short-range structures renders it particularly attractive for the characterization of systems, such as amorphous materials and liquids, including solutions, suspensions, emulsions and melts, without a long-range order.<sup>1</sup> Studies on the electronic structure and local bonding in these systems are of multi-disciplinary relevance, including chemistry (e.g. catalysis, synthesis, self-assembly, and electrochemistry), biology (membrane function and metalloproteins), physics (super- and semiconductors, magnetism, and glasses), environ-

mental science (soil remediation and waste), materials science (functional materials, biomaterials, and ceramics) and engineering (separations, corrosion, electronics, and photonics).<sup>1</sup>

For X-ray absorption edges in the hard X-ray range (photon energies above 5 keV), XAS is a versatile technique for probing reactions and physical transformations *in situ* and *operando* because hard X-rays readily penetrate air and many X-ray window materials. Thus, the probing of many high temperature and pressure sample environments using hard X-rays have been reported, e.g. for hydrothermal and catalytic applications.<sup>2,3</sup>

For X-ray photon energies below 5 keV, air and window materials significantly attenuate the photon flux. The photon energy range between 1 and 5 keV (often referred to as the 'tender' X-ray range) is of current interest because it includes the K absorption edges of important elements in the 3rd and 4th period (from Na to Ca) as well as the L-edges of elements ranging from Zn to Cs. To minimize X-ray absorption by ambient gases, the sample environment is either flushed with a weakly absorbing gas (typically He) or evacuated using vacuum pumps. X-ray transparent windows are required for incident X-rays to reach the sample and also for transmitted/

<sup>a</sup> School of Chemical and Process Engineering, University of Leeds, Leeds, LS2 9JT, UK. E-mail: s.l.m.schroeder@leeds.ac.uk

<sup>b</sup> School of Design, University of Leeds, Leeds, LS2 9JT, UK

<sup>c</sup> Diamond Light Source, Didcot, Oxfordshire OX11 0DE, UK

<sup>d</sup> Infineum UK Ltd, Abingdon, Oxfordshire, OX13 6BB, UK.

E-mail: colin.willis@infineum.com

† Electronic supplementary information (ESI) available. See DOI: 10.1039/c8re00207j



fluorescent X-rays to reach the detector. Window materials that are suitably transparent for applications in the tender X-rays range include polyimide, Mylar, polymers and ultrathin beryllium; however, they have limited scope for experiments at elevated temperatures and pressures and in the presence of chemical reactants that may corrode, dissolve or decompose the window materials.<sup>4</sup> These requirements restrict the scope for *in situ* and/or *operando* reactor design, often rendering reaction conditions, for example operating temperature, pressure and multi-component heterogeneous processes in liquid phase, a poor model of the actual process of interest. Nevertheless, *operando* electrochemical cells have been developed for measurements at the S K- and P K-edges.<sup>5,6</sup>

For multiphase liquid–solid dispersion samples, it is preferable to have windowless probing. When a process involves nucleation, adsorption or precipitation of solid particles, deposition on the window materials can occur, resulting in XAS analysis of an unrepresentative aliquot of the reaction mixture.<sup>7</sup> For tender X-ray experiments, fluorescence-yield (FY) detection is particularly affected compared with transmission as it is surface rather than bulk sensitive. Windowless probing of multiphase samples avoids these problems and has been explored for a variety of X-ray sample environments, including supported and hanging droplets,<sup>8,9</sup> levitated droplets,<sup>10</sup> static solutions<sup>11,12</sup> and liquid-jets.<sup>13</sup>

We developed an inexpensive and versatile ambient pressure cell with the capability of probing a wide range of dynamic gas–liquid–solid systems through windowless liquid-jet operation. Operating under an He flow at atmospheric pressure facilitates measurements in the tender X-ray range above 3–4 keV. The cell was constructed from standard vacuum parts and fittings for gas or liquid streams. After X-ray probing, the liquid volume is collected and fed back to the supply vessel, facilitating an external sampling loop for the continuous monitoring of reactions without loss in sample volume. This provides the capability for *operando* process studies using large reaction vessels with control over the gas environment and temperature. To allow studies of viscous and/or multiphase systems in the presence of solid particulates, the inner diameter and length of the jet inlet tube can be varied and optimized. High flow rates also enable short residence time in the flow loop, with associated minimization of heat losses and radiation damage by absorbed X-rays.

Herein, we demonstrate the construction and operation of the cell. We present data for the reactive crystallization of  $\text{CaCO}_3$  from an aqueous calcium hydroxide ( $\text{Ca}(\text{OH})_2$ ) dispersion at 28 °C using the liquid-jet configuration with a controlled gas phase environment. Specifically, in this study, the system is a ‘dispersion-jet’ rather than a ‘liquid-jet’, but we use the term ‘liquid-jet’ to emphasize the fact that our system uses a pressurized jet system in the same way as conventional liquid-jet sampling environments.<sup>14</sup> We complement this work by following the formation of  $\text{CaCO}_3$  at the gas–liquid interface between a sessile droplet of a saturated  $\text{Ca}(\text{OH})_2$  solution with  $\text{CO}_2$  dosed directly into the analysis chamber.

Finally, it should be mentioned that in the soft X-ray range (at photon energies below 1 keV), the absorption of photons by air is so strong that experiments are traditionally performed in vacuum chambers. For studies of liquids, transmission flow cells were constructed, in which a few hundred nm-thick liquid sample is separated from the vacuum environment using two windows.<sup>15,16</sup> The currently most common form of liquid sample delivery into vacuum chambers is *via* liquid-microjets, with fluorescence- or electron-yield detection of the absorption spectra.<sup>14</sup> Moreover, *in situ* and *operando* liquid cells for soft X-rays have recently been developed for electrochemical, heterogeneous catalysis and more recently, for high pressure applications.<sup>4,17–19</sup> The setup reported herein was inspired by these microjet cells.

## 2. Experimental

### 2.1 Material

Geological  $\text{CaCO}_3$  powder (calcite,  $\geq 99\%$ , Sigma Aldrich, UK) and  $\text{Ca}(\text{OH})_2$  (94%, L’Hoist, UK) were used. Deionized water was utilized throughout the experiments. He,  $\text{N}_2$  and  $\text{CO}_2$  (BIP purity) from Air Products were used.

### 2.2 XAS experiments

XAS measurements were carried out at Diamond Light Source, UK on beamline B18 at the Ca K-edge (*ca.* 4 keV).<sup>20</sup> An Si (111) double crystal monochromator was used. The synchrotron was operated at 3 GeV with a ring current of 300 mA. For the recycling liquid-jet experiments, the beam footprint was 800  $\mu\text{m}$  in height and 600  $\mu\text{m}$  in width. For the sessile droplet experiments, the beam footprint was 1.2 mm in height and 1.8 mm in width. The dwell time was 0.14 second  $\text{eV}^{-1}$  for the droplet measurements and 0.2 second  $\text{eV}^{-1}$  for the liquid-jet measurements. Measurement of each spectrum took one to three minutes. The liquid phase spectra were collected in the FY mode using a 4-element SII Vortex silicon-drift detector with XSPRESS3 electronics. The solid phase reference samples  $\text{Ca}(\text{OH})_2$  and calcite were spread on double-sided carbon tapes and measured using gas flow total electron yield (TEY) detection. A metal electron collector was positioned 1 cm from the sample and biased at +63 V using a battery box.

All experimental data were processed using Athena in the Demeter software package.<sup>21</sup> The changes in sample compositions due to carbonation were quantified using linear combination fitting (LCF) of X-ray absorption near edge structure (XANES) spectra over the energy range of 4000 to 4130 eV. The components used for the LCF were the spectra of solid phase calcite and  $\text{Ca}(\text{OH})_2$  as well as the spectrum of a saturated 18.8 mM  $\text{Ca}(\text{OH})_2$  or  $\text{Ca}^{2+}$  solution, where mM indicates  $\text{mmol L}^{-1}$ .

### 2.3 The environmental cell/the analysis chamber

The environmental cell was constructed from commercially available standard parts including ConFlat (CF) vacuum parts, polyimide films and standard glassware to ensure ease



of assembly and reproducibility. The construction of the environmental cell was based on a CF40 flange ultrahigh vacuum cube. The schematics of the setup shown in Fig. 1 and 2 show that the incident X-rays entered *via* a windowless port. At the opposite end of the cell, a 75  $\mu\text{m}$  thick polyimide window was positioned for X-ray transmission measurements, which is required for alignment of the sample in the X-ray beam. A second polyimide window was fixed to a port located perpendicular to the direction of the X-ray beam, which allowed for the positioning of an external fluorescence-yield detector with minimal air path (Fig. 2). Accordingly, the fluorescence detector was positioned at approximately 40 mm away from the sample in the center of the cell. The other 90° port held a fast-entry load lock, which also served as a viewport for visible monitoring with a camera. A 5 × CF16 cluster flange mounted on top permitted the addition of various feedthroughs including the helium gas inlet, which was fed through a 1/8" Swagelok fitting and a glass tubing, which was fed through a 1/4" quick-connect adaptor single fitting (Kurt J. Lesker). The analysis chamber was maintained in a helium environment to minimize absorption in the tender X-ray range. All other unused ports were closed off with blank flanges to maintain a closed system.

The cell was attached to the beamline *via* a flexible KF40 bellow positioned after the ion chamber that monitored the intensity of the incident X-ray beam. The bellow gave flexibility to align the position of the environmental cell relative to the X-ray beam. The environmental cell was mechanically supported to the beamline *via* metal posts attached to a motorized stage. The cell is also portable, enabling users to move it between home institutions and synchrotron light sources and/or between beamlines.

The cell was operated in two configurations, either as a recycling liquid-jet cell or as a droplet cell, as follows.

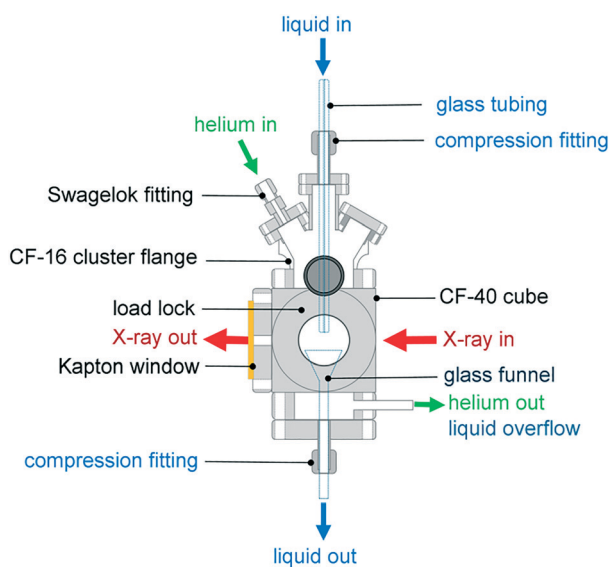


Fig. 1 The environmental cell dedicated to liquid-jet and droplet operation under a controlled gas environment.

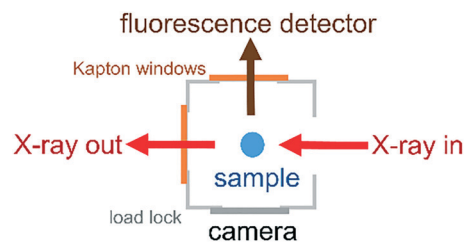


Fig. 2 Aerial view of the CF40 cube showing the positions of the fluorescence detector, camera and X-ray beam path.

**Recycling liquid-jet configuration.** In the recycling liquid-jet configuration, the sample was continuously pumped through the cell (up to 370 mL min<sup>-1</sup>) and recycled back to a glass reactor using two peristaltic pumps (Watson Marlow 520, Fig. 3). Viton flexible tubing (Cole Parmer, L/S 16, shore hardness 75, inner diameter 3.2 mm, and wall thickness 1.6 mm) was used for the sample loop due to its good chemical and mechanical resistance. The dispersions were introduced into the cell in the form of a 0.8 mm diameter liquid-jet stream from a capillary bore glass tubing (length 190 mm, outer diameter 6 mm, and inner diameter 0.8 mm). The glass tubing was fixed to the cell using a CF to quick-connect coupling single adaptor (Kurt J. Lesker) positioned at the top of the cube. X-ray absorption spectra from the jet were measured at approximately 5 mm below the tip of the glass tubing. The probed area of the liquid-jet appeared to have a cylindrical smooth flow. At positions further from the tip of the glass tubing, the liquid-jet was more strongly influenced by the pulsating signals from the rolling mechanism of the peristaltic pump heads. The residence time across the 4 m sampling loop was less than 5 seconds, which was significantly shorter than the 3 min measurement duration of each spectrum.

To collect the sample volume for recycling, a custom-made glass funnel (top cone diameter 25 mm and stem diameter 6 mm) was fixed at the bottom of the cube. The glass stem was fed through a CF to quick-connect coupling single adaptor to fit the CF40 cube. All materials used for the construction of the flow loop were compatible with organic solvents, including the Viton tubing for use with the peristaltic

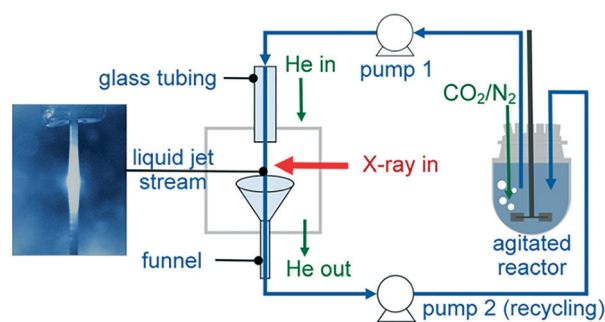


Fig. 3 Recycling liquid-jet configuration for monitoring the *operando* carbonation of a Ca(OH)<sub>2</sub> aqueous dispersion at the Ca K-edge.





pump, Viton gaskets, glass reactor, glass tubing and stainless steel cell body.

To demonstrate the capability of the liquid-jet cell, we followed the *operando* carbonation of a supersaturated aqueous dispersion of  $\text{Ca}(\text{OH})_2$  (75 mM). 750 mL of the dispersion was mixed in a 1 L glass reactor using an overhead stirrer at 400 rpm. The CF40 cube chamber was constantly flushed with 1 L  $\text{min}^{-1}$  helium to maximize X-ray transmission. Overall, the small volume of the CF40 cube required less than ten minutes to be purged by helium gas. Prior to the XAS measurements and the carbonation reaction, the reaction mixture was purged with 30  $\text{mL min}^{-1}$  of  $\text{N}_2$  gas to minimize the influx of atmospheric  $\text{CO}_2$ . For the carbonation reactions, the  $\text{Ca}(\text{OH})_2$  dispersion was purged with 57  $\text{mL min}^{-1}$   $\text{CO}_2$  and 30  $\text{mL min}^{-1}$   $\text{N}_2$ . After 20 min of carbonation, the  $\text{CO}_2$  flow was stopped. To ensure complete monitoring of the reaction between  $\text{Ca}(\text{OH})_2$  and the reactant ( $\text{CO}_2$ ), XAS measurements were continued up to 15 min after the  $\text{CO}_2$  flow was terminated. During reaction, the content of the glass vessel was maintained at  $28 \pm 2$  °C using a temperature feedback loop consisting of a thermocouple, heating mantle, cooling coil and West N4400 temperature controller. The temperature regulation system was also a safety feature to prevent overheating during the exothermic carbonation reaction. Before carrying out the experiments, the sampling loop was flushed thoroughly with dilute acid and deionized water.

**Sessile droplet configuration.** Using the droplet configuration, a sessile droplet was formed at the end of a glass tubing (length 190 mm, outer diameter 6 mm, and inner diameter 4 mm) fed through the quick-connect coupling positioned at the bottom of the CF40 cube. A clear saturated aqueous solution of 18.8 mM  $\text{Ca}(\text{OH})_2$  was injected using a syringe *via* a 1/8" PTFE tubing to produce a sessile droplet at the end of the glass tubing (Fig. 4). During the carbonation reaction, 10  $\text{mL min}^{-1}$  of 10%  $\text{CO}_2$  in helium was introduced into the CF40 cube.

### 3. Results

The liquid-jet and droplet environmental cells were tested by monitoring the Ca K-edge, following the formation of  $\text{CaCO}_3$  from  $\text{Ca}(\text{OH})_2$  in the presence of  $\text{CO}_2$  gas. These experiments demonstrated the ability of the cell: (i) to handle tender X-rays ( $\sim 4$  keV) through use of an He environment, (ii) to accommodate multiphase systems, as exemplified by the three-

phase gas–liquid–solid system; and (iii) to generate X-ray absorption spectra of sufficient quality to monitor the progress of the carbonation reaction.

#### 3.1 Recycling liquid-jet

The XANES spectra in Fig. 5 show the gradual transformation of  $\text{Ca}(\text{OH})_2$  to calcite over a period of 30 min. This demonstrates the successful handling of a multiphase system containing gas, liquid and dispersion for XAS analysis at the Ca K-edge. Before carbonation, LCF analysis of the XANES spectrum showed that within the volume of the stream probed, there was a mixture of 33% dissolved  $\text{Ca}^{2+}$  species and 67%  $\text{Ca}(\text{OH})_2$  dispersion (Fig. 6). After  $\text{CO}_2$  was introduced into the system, the composition of  $\text{Ca}(\text{OH})_2$  decreased steadily with time. For the first 12 minutes of carbonation, the content of  $\text{Ca}^{2+}$  ions fluctuated at around 40% while the supply of  $\text{Ca}(\text{OH})_2$  gradually decreased (Fig. 7). After 12 minutes, the content of  $\text{Ca}^{2+}$  ions started to decrease. The decrease in  $\text{Ca}(\text{OH})_2$  and  $\text{Ca}^{2+}$  ions was accompanied by the formation of calcite, as evident from the gradual increase in the intensity of the shoulder at 4045 eV of the pre-edge region and the modulation at the 4060 eV region (Fig. 5). At the end of the carbonation reaction, calcite dominated the composition of the system. Overall, the LCF analysis of the liquid-jet system suggests a three-step reaction mechanism: (i) the dissolution of solid  $\text{Ca}(\text{OH})_2$  to give aqueous  $\text{Ca}^{2+}$  ions; (ii) the dissolution of  $\text{CO}_2$  gas to give aqueous  $\text{CO}_3^{2-}$  ions; and (iii) the reaction of the aqueous  $\text{Ca}^{2+}$  and  $\text{CO}_3^{2-}$  ions to form solid calcite.

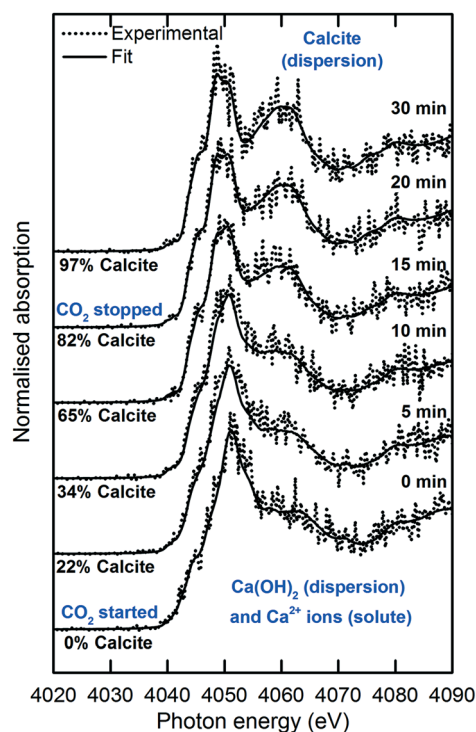


Fig. 5 Time-dependent Ca K-edge XANES spectra of the *operando* carbonation of 75 mM  $\text{Ca}(\text{OH})_2$  using the recycling liquid-jet configuration.

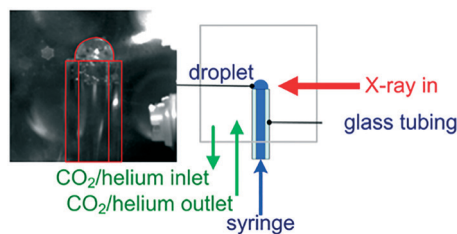


Fig. 4 Sessile droplet configuration for monitoring the *operando* carbonation of a  $\text{Ca}(\text{OH})_2$  solution at the Ca K-edge.



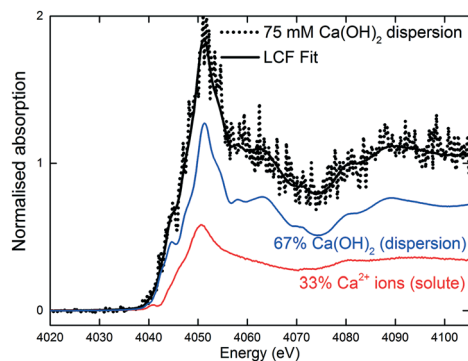


Fig. 6 LCF of the 75 mM aqueous  $\text{Ca(OH)}_2$  dispersion in the liquid-jet configuration before  $\text{CO}_2$  was introduced.

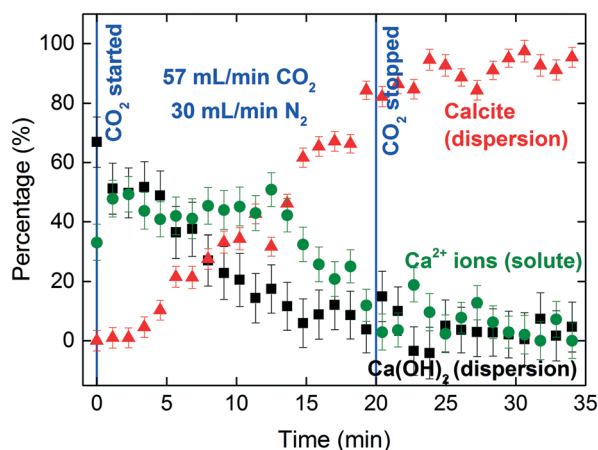


Fig. 7 Time-dependent composition profile of  $\text{Ca(OH)}_2$  dispersion, dissolved  $\text{Ca}^{2+}$  ions and calcite dispersants during the *operando* carbonation of 75 mM  $\text{Ca(OH)}_2$  using the recycling liquid-jet configuration. The composition profile was obtained by deconvoluting the Ca K-edge XANES spectra using linear combination fitting.

### 3.2 Sessile droplet

The sessile droplet allowed observation of the direct formation of calcite from dissolved  $\text{Ca}^{2+}$  ions but at the gas–liquid interface (Fig. 8 and 9). With the aid of a high-resolution camera (Fig. 4), we observed the formation of an inhomogeneous opaque film across the surface of the droplet as carbonation progressed. The visible film is likely to be a thin layer of calcite formed at the gas–liquid interface by carbonation, as evidenced from the formation of a shoulder at 4045 eV and the modulation at 4060 eV region. The solid calcite product appeared to adhere to the surface of the droplet due to interfacial tension.

The signal-to-noise quality of the XANES spectra is better in the sessile droplet setup compared to that from the liquid-jet setup. This is reflected in the larger error bars in the LCF results for the liquid-jet system compared with the droplet system (Fig. 7 and 9, respectively). Even though the dwell time for the measurements of the liquid-jet spectra was longer compared to that for the sessile droplet spectra, pulsation of the jet flow and suspended solid particles passing through the X-ray beam contributed to lowering the signal-to-noise ra-

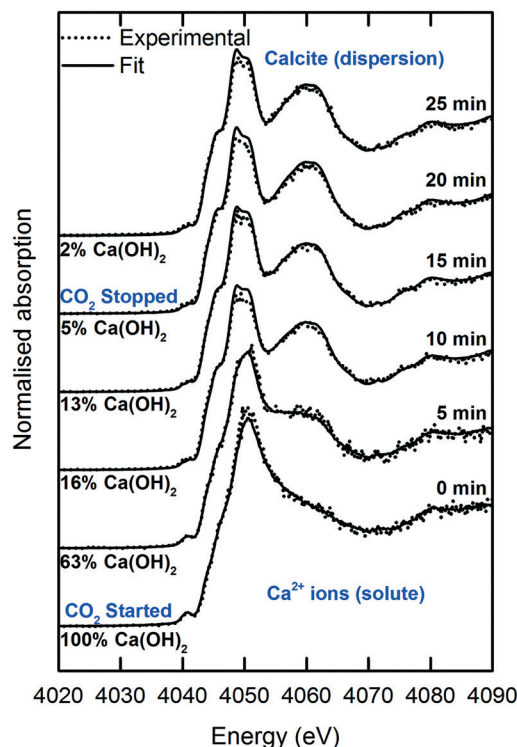


Fig. 8 Time-dependent Ca K-edge XANES spectra of the *operando* carbonation of 18.8 mM  $\text{Ca(OH)}_2$  using the sessile droplet configuration.

tio of the liquid-jet spectra. In contrast, the sessile droplet was initially a clear solution, which remained relatively stable in its position, aside from the gradual shrinkage in the droplet due to evaporation.

It should be noted that the initial  $\text{Ca(OH)}_2$  concentration used in the droplet and the liquid-jet experiments was different (Fig. 10). The solution in the droplet experiment was a saturated solution with 18.8 mM  $\text{Ca(OH)}_2$ , *i.e.*, a clear solution containing only dissolved  $\text{Ca}^{2+}$  ions and no dispersed  $\text{Ca(OH)}_2$  particulates. For the liquid-jet experiment, we used a

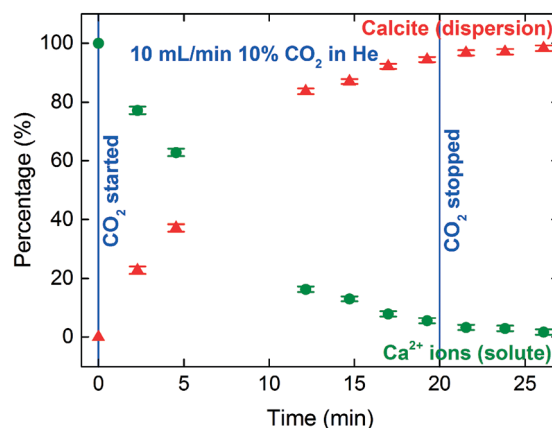


Fig. 9 The composition profile of  $\text{Ca}^{2+}$  and calcite during the *operando* carbonation of 18.8 mM  $\text{Ca(OH)}_2$  using the sessile droplet configuration. The composition profile was obtained by deconvoluting the Ca K-edge XANES spectra using linear combination fitting.



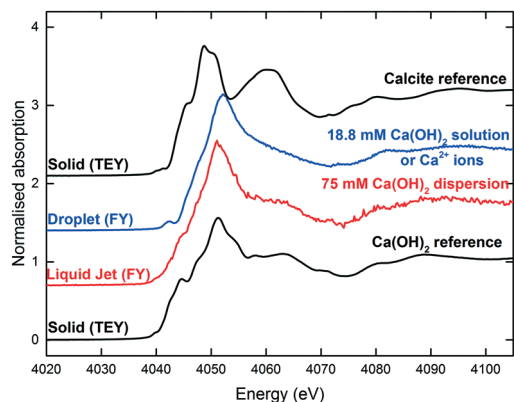


Fig. 10 The reference Ca K-edge XANES spectra. The sessile droplet spectrum was averaged over 13 spectra. The liquid-jet spectrum was averaged over 17 spectra.

75 mM  $\text{Ca(OH)}_2$  dispersion, representing a saturated  $\text{Ca}^{2+}$  solution in contact with  $\text{Ca(OH)}_2$  dispersion. Therefore, the initial spectra for the two systems were different since the spectral features of  $\text{Ca}^{2+}$  ions and  $\text{Ca(OH)}_2$  are different (Fig. 10).

In addition, the calcite formation profile appeared to be different for the liquid-jet and droplet systems (Fig. 7 and 9, respectively). The liquid-jet system appeared to have an upward convex calcite profile; whereas, the sessile droplet system had a downward convex calcite profile. The difference was particularly obvious after five minutes of introducing  $\text{CO}_2$  into the system, where 37% of the reactant was converted to calcite in the droplet system. On the other hand, in the liquid-jet configuration, only 10% of the reactant was converted to calcite. The different calcite formation profiles observed in the two systems may be due to the different mixing behaviors in both systems. In the droplet configuration, insoluble calcite particles formed at the gas–liquid interface and remained suspended at the surface of the droplet by interfacial tension. In contrast, in the liquid-jet configuration, the calcite particles formed were mixed with the dispersion samples. Considering that FY detection is sensitive towards the top hundred  $\mu\text{m}$  layer of a sample and that calcite accumulated at the surface of the droplet but not at the surface of liquid-jet, the droplet system appeared to have a higher concentration of calcite than the liquid-jet system.

In addition, the calcite formation profile may be influenced by the different reaction pathways in both the droplet and liquid-jet systems. In the saturated solution in the droplet system, calcite was formed directly from  $\text{Ca}^{2+}$  ions and the reaction was limited by the diffusion of  $\text{CO}_2$ . On the other hand, in the liquid-jet system containing dissolved  $\text{Ca}^{2+}$  ions and  $\text{Ca(OH)}_2$  dispersion, an additional  $\text{Ca(OH)}_2$  dissolution step was involved, and thus the reaction may be limited by both the  $\text{Ca(OH)}_2$  dissolution rate and  $\text{CO}_2$  diffusion.

## 4. Discussion

Prior to carbonation, the XANES spectrum of the soluble  $\text{Ca}^{2+}$  species (as exemplified by the saturated  $\text{Ca(OH)}_2$  solution in

the droplet configuration in Fig. 8 and 10) is reminiscent of the spectra of  $\text{Ca}^{2+}$  species with low symmetry coordination polyhedra, e.g. dilute  $\text{CaCl}_2$  aqueous solution<sup>22</sup> and amorphous  $\text{CaCO}_3$ .<sup>23</sup> The spectral characteristics of  $\text{Ca}^{2+}$  ions include: (i) the  $1s \rightarrow 3d$  pre-edge feature at 4040.7 eV, which is a forbidden transition in the octahedral symmetries, but can be present in distorted coordination polyhedra, (ii) the absence of the  $1s \rightarrow 4p$  shoulder at 4045 eV, and (iii) an intense peak at 4050.5 eV arising from the Ca–O scattering path.<sup>22</sup>

Calcite has more distinctive spectral features compared to  $\text{Ca}^{2+}$  ions due to the ordered coordination polyhedra in the calcite crystal. The spectrum of calcite is readily distinguishable from the spectra of the other anhydrous polymorphs of  $\text{CaCO}_3$ , namely aragonite and vaterite.<sup>23–25</sup> The spectral characteristics of calcite include: (i) a  $1s \rightarrow 3d$  split pre-edge peak at 4040.7 eV, which arises from admixing of p-states with the 3d final state, (ii) a  $1s \rightarrow 4p$  shoulder at 4045 eV and (iii) intense peaks at 4050 and 4060 eV. Previous studies on the formation of  $\text{CaCO}_3$  from aqueous  $\text{Ca(OH)}_2$  systems mostly focused on the modification of the morphology of calcite particles by varying the reaction conditions.<sup>26</sup> It should be noted that the polymorphic form of the  $\text{CaCO}_3$  products formed is known to be a complex function of pH, concentration, temperature, stirring rate, and the type and concentration of additives and reactants.<sup>27</sup>

A comparison of the capabilities and limitations of the droplet and liquid-jet configurations is given in Table 1. We demonstrated that the liquid-jet configuration allows handling of a multiphase gas–liquid–solid system. This capability was achieved by having a relatively large bore diameter of 0.8 mm for the tubing that delivered the jet and by flowing the dispersion at a suitably high flow rate of  $370 \text{ mL min}^{-1}$ . These features helped to minimize pulsation of the liquid-jet stream propagated from the mechanical movement of the peristaltic pump rollers and minimize the probability of blockage of the sampling loop by the dispersion. When the composition of the solution or dispersion is changed, the liquid-jet flow rate and the bore size of the liquid-jet tubing may need to be adjusted accordingly to cater for the change in sample viscosity. Previous studies<sup>28,29</sup> described a windowless recycling liquid-jet cell for *in situ* monitoring the synthesis of nanoparticles at ambient pressure using synchrotron small angle X-ray scattering (SAXS) and XAS techniques. These studies<sup>28,29</sup> used hard X-rays, which allowed the straightforward incorporation of a recycling stream at ambient conditions. However, these setups are open systems without a controlled gas environment, which prohibits their use in the tender X-ray range.

Droplet cells can be used to measure the early stages of homogeneous nucleation since turbulence and mechanical disturbances are kept minimal in the static configuration. Actually, the droplet configuration is a popular choice for handling liquid samples, particularly where contact of liquid with the wall of a sample vessel or any other surface will affect the outcome of the experiment, e.g. when high energy defects on windows and walls may act as a site for heterogeneous nucleation.<sup>9,30</sup> It has been shown that a double droplet



**Table 1** Capabilities and limitations of the droplet and liquid-jet configurations used in this study

	Droplet	Liquid-jet
Sampling mode	Static single or double droplet. Minimal mechanical disturbances with a defect-free platform	Dynamic liquid-jet stream. Mechanically agitated in the glass vessel and in the recycling sampling loop
Windowless sampling?	Yes	Yes
Solvent evaporation	Solvent evaporation will cause the sample to shrink and move out from the beam path	Negligible effects
Volume requirement	Small droplet volume (<1 mL) with a small sample reservoir on the 5 mL scale	Sample reservoir in a large reaction vessel in the 500–1000 mL scale with a 30 mL liquid-jet sampling loop
Gas-sample interaction	At the droplet gas–liquid interface. There will be gas diffusion gradient across the surface normal direction	In a well-mixed reaction vessel
Immiscible solvents	Possible to study but in separated phases, making use of the hanging and sessile double droplet configurations	Possible to study in the form of a well-mixed sample
Temperature control	Currently not available but possible	Currently tested up to 60 °C in the reaction vessel
Analysis chamber pressure	Ambient pressure only. Limited by mechanical properties of the windows	
X-ray energy range	Tender and hard X-rays. Currently, above 3–4 keV but can be adapted for slightly lower energies	

configuration provides a free-standing liquid–liquid interface for two immiscible solvents, which served as a defect-free platform for nanoparticle synthesis studies.<sup>9,31</sup> This double droplet configuration can incorporate electrochemical control of the liquid–liquid interface to vary reaction rates,<sup>8,9</sup> and thus the cell described in the present study will enable such experiment with minimal modification. Acoustic levitation of droplets<sup>10</sup> also offers a fully windowless option to study liquids.

Compared to the liquid-jet configuration, the droplet configuration demands a much smaller reservoir volume compared (in the order of several mL vs. few hundred mL). Thus, the droplet cell is ideal in circumstances where sample volumes are limited. It should be noted that a microfluidic flow cell<sup>32</sup> only require a small amount of sample in the order of a few hundred  $\mu\text{L}$  or mL. The samples are contained within the cell, rendering the microfluidic cell optimal for studying synthesis involving volatile and explosive substances. However, a microfocus X-ray beam may be required to perform XAS measurements in a microfluidic cell.

For the droplet configuration, the aqueous  $\text{Ca}(\text{OH})_2$  solution was stable over the duration of the XAS measurements. Additional procedures to maintain a stable droplet size was not required. However, when monitoring over an extended duration and when a volatile organic solvent is used, solvent evaporation can be an issue since the droplet may gradually shrink and move out from the beam path. To mitigate this, a slow sample flow rate can be continuously injected using a syringe pump to maintain a constant droplet size. Alternatively, the droplet size can be maintained by saturating the gas environment with solvent vapour using a humidity feedback loop comprising of a humid carrier gas stream, a humidity monitor and a humidity controller.

In the liquid-jet configuration, the dispersion sample in the glass reaction vessel was maintained at 28 °C during the

carbonation reaction. The setup can be operated at even higher temperatures and was tested for reactions up to 60 °C. Besides maintaining the operating temperature, the temperature control loop helped to prevent sample overheating during the exothermic carbonation reaction. For the reaction at 28 °C, temperature loss across the thick-wall Viton tubing was likely to be negligible. The main source of heat loss along the sampling loop would be at the liquid-jet *via* convective and radiative heat loss, which is also likely to be negligible since the liquid-jet stream had less than 1 millisecond of exposure to the helium environment before intersecting with the position of the X-rays beam. For applications at higher temperature, the flexible tubing and metal structures of the X-ray sampling environment may need to be heated and insulated to ensure minimal heat loss from the sampling loop. Maintaining a constant temperature along the sampling line is important since the reaction kinetics and solubility may be affected by temperature. A decrease in solubility at lower temperatures may lead to solute deposition and blockages in the sample delivery line. For the droplet configuration, the sample can be heated convectively by a stream of hot gas and by adding heating tapes around the metal structures of the droplet sampling environment. To complete the temperature feedback loop, a thermocouple can be implemented in the droplet delivery tubing with a temperature controller.

Both the liquid-jet and sessile droplet cells described in this study were not optimized for reactions at elevated pressures. In that case, a new structure will be necessary, most likely making use of windowed cells to contain a pressurised environment. The glass vessel in the liquid-jet configuration will also need to be replaced by pressure-rated metal reactors.

The cells were initially built with the aim of studying the  $\text{CaCO}_3$  crystallisation processes *in situ* using XAS, an area that is yet to be fully explored.<sup>33</sup> The capabilities of the





liquid-jet and droplet systems were tested at the Ca K-edge; however, the long-term goal is to optimize them further to allow measurements below 4 keV. The polyimide window material and He environment in the cells described in this study were suitable for hard X-rays and part of the tender X-rays region. Only some modifications should be necessary to enable experiments in the softer range, for example P, S and Cl K-edges. The modifications required for accessing softer X-rays include thinner polyimide windows and direct attachment of the FY detector to the He-filled cell since even 1 cm of air significantly attenuates fluorescence signals in the softer energy range. Both cells used in this study are not suitable for transmission measurements at the Ca K-edge because X-rays at 4 keV will be fully absorbed across the 0.8 mm diameter liquid-jet and 6 mm diameter droplet.

The liquid-jet and droplet configurations described in this study can be either directly used or adapted for applications in nucleation, crystallization, complex nanoparticle synthesis and photocatalytic reactions. In this study, we demonstrated their applications in the carbonation of aqueous  $\text{Ca}(\text{OH})_2$  systems. Some other examples of *in situ* studies on calcium systems include SAXS study of the formation of  $\text{CaCO}_3$  using a recycling liquid-jet cell<sup>34</sup> and XANES study of the formation of calcium phosphate clusters using a static cell.<sup>35</sup> Using these sample environments, the interdependence of the different stages of particle formation (pre-nucleation, early nucleation and growth) with reaction conditions and solvents can be studied. Since both the liquid-jet and sessile droplet configurations are constructed for operation at atmospheric pressure, there may be limited scope for *operando* applications in the some industrial processes and catalytic reactions that require operation at elevated pressure.

## Conclusions

We constructed a versatile cell that permits the windowless probing of dynamic processes in liquid dispersions and solutions by XAS, notably including the photon energy range in the tender X-ray range above 4 keV and in the hard X-ray range. The cell can be operated in the liquid-jet or droplet configuration, while also allowing mounting of solid samples. *Operando* time-dependent measurements during the carbonation of aqueous  $\text{Ca}(\text{OH})_2$  were demonstrated for both the liquid-jet and droplet cell operations. The Ca K-edge XAS data quantified the composition of the reaction system during the transformation of  $\text{Ca}(\text{OH})_2$  to calcite in the presence of  $\text{CO}_2$ . These gas–solid–liquid studies also demonstrated the capability of the cells to monitor multiphase systems. For liquid-jet operation, recycling minimized the loss of sample volume. Therefore, this system opens an inexpensive avenue to study multiphase systems, widening the applications of *operando* XAS to study complex colloidal systems, including viscous Newtonian and non-Newtonian systems and heterogeneous nucleation and crystallization processes.

## Conflicts of interest

There are no conflicts to declare.

## Acknowledgements

The authors thank Diamond Light Source for the award of beamtime at B18 under proposal number SP15850-1 and SP14673-1. The authors would also like to thank Professor Peter Heggs, University of Leeds for the constructive discussion on temperature control. TAK gratefully acknowledges the financial support from Infineum UK and EPSRC Centre for Doctoral Training in Complex Particulate Products and Processes (EP/L015285/1). SLMS would like to thank Royal Academy of Engineering, Diamond and Infineum UK for support of the Bragg Centenary chair. SYC is grateful to Infineum UK, AstraZeneca, Diamond Light Source for the financial support. All data supporting this study are provided either in the results section of this paper or in the ESI† accompanying it.

## References

- 1 J. A. V. Bokhoven and C. Lamberti, *X-ray Absorption and X-ray Emission Spectroscopy: Theory and Applications*, John Wiley & Sons, 2016.
- 2 J.-D. Grunwaldt, M. Ramin, M. Rohr, A. Michailovski, G. R. Patzke and A. Baiker, *Rev. Sci. Instrum.*, 2005, **76**, 054104.
- 3 J. L. Fulton, J. G. Darab and M. M. Hoffmann, *Rev. Sci. Instrum.*, 2001, **72**, 2117–2122.
- 4 R. Qiao, Y. Xia, X. Feng, J. Macdougall, J. Pepper, K. Armitage, J. Borsos, K. G. Knauss, N. Lee, A. Allézy, B. Gilbert, A. A. MacDowell, Y.-S. Liu, P.-A. Glans, X. Sun, W. Chao and J. Guo, *Rev. Sci. Instrum.*, 2018, **89**, 013114.
- 5 Y. Ye, A. Kawase, M.-K. Song, B. Feng, Y.-S. Liu, M. Marcus, J. Feng, E. Cairns, J. Guo and J. Zhu, *Nanomaterials*, 2016, **6**, 14.
- 6 S. Schmidt, S. Sallard, C. Borca, T. Huthwelker, P. Novák and C. Villevieille, *Chem. Commun.*, 2018, **54**, 4939–4942.
- 7 L. N. Nchari, G. A. Hembury, A. M. Beesley, D. J. Meehan, N. Tsapatsaris, M. Hudson, M. Thomason and S. L. M. Schroeder, *J. Phys.: Conf. Ser.*, 2009, **190**, 0121556.
- 8 S. G. Booth, A. Uehara, S. Y. Chang, J. F. W. Mosselmans, S. L. M. Schroeder and R. A. W. Dryfe, *J. Phys. Chem. C*, 2015, **119**, 16785–16792.
- 9 Y. Gründer, J. F. W. Mosselmans, S. L. M. Schroeder and R. A. W. Dryfe, *J. Phys. Chem. C*, 2013, **117**, 5765–5773.
- 10 S. E. Wolf, J. Leiterer, M. Kappl, F. Emmerling and W. Tremel, *J. Am. Chem. Soc.*, 2008, **130**, 12342–12347.
- 11 M. L. Schlossman, D. M. Mitrinovic, Z. Zhang, M. Li and Z. Huang, *Synchrotron Radiat. News*, 1999, **12**, 53–58.
- 12 I. Watanabe, H. Tanida, S. Kawauchi, M. Harada and M. Nomura, *Rev. Sci. Instrum.*, 1997, **68**, 3307–3311.
- 13 J. Polte, R. Erler, A. F. Thunemann, F. Emmerling and R. Kraehnert, *Chem. Commun.*, 2010, **46**, 9209–9211.
- 14 J. W. Smith and R. J. Saykally, *Chem. Rev.*, 2017, **117**, 13909–13934.
- 15 N. Huse, T. K. Kim, L. Jamula, J. K. McCusker, F. M. F. de Groot and R. W. Schoenlein, *J. Am. Chem. Soc.*, 2010, **132**, 6809–6816.



- 16 S. Schreck, G. Gavrila, C. Weniger and P. Wernet, *Rev. Sci. Instrum.*, 2011, **82**, 103101.
- 17 C. Schwanke, R. Golnak, J. Xiao and K. M. Lange, *Rev. Sci. Instrum.*, 2014, **85**, 103120.
- 18 C. Schwanke, L. Xi and K. M. Lange, *J. Synchrotron Radiat.*, 2016, **23**, 1390–1394.
- 19 H. Yuzawa, M. Nagasaka and N. Kosugi, *J. Phys. Chem. C*, 2015, **119**, 7738–7745.
- 20 A. J. Dent, G. Cibir, S. Ramos, A. D. Smith, S. M. Scott, L. Varandas, M. R. Pearson, N. A. Krumpa, C. P. Jones and P. E. Robbins, *J. Phys.: Conf. Ser.*, 2009, **190**, 012039.
- 21 B. Ravel and M. Newville, *J. Synchrotron Radiat.*, 2005, **12**, 537–541.
- 22 J. L. Fulton, S. M. Heald, Y. S. Badyal and J. M. Simonson, *J. Phys. Chem. A*, 2003, **107**, 4688–4696.
- 23 R. S. K. Lam, J. M. Charnock, A. Lennie and F. C. Meldrum, *CrystEngComm*, 2007, **9**, 1226–1236.
- 24 L. Brinza, P. F. Schofield, M. E. Hodson, S. Weller, K. Ignatyev, K. Geraki, P. D. Quinn and J. F. W. Mosselmans, *J. Synchrotron Radiat.*, 2014, **21**, 235–241.
- 25 Y. Politi, Y. Levi-Kalishman, S. Raz, F. Wilt, L. Addadi, S. Weiner and I. Sagi, *Adv. Funct. Mater.*, 2006, **16**, 1289–1298.
- 26 M. Ukrainezyk, J. Kontrec, V. Babić-Ivančić, L. Brečević and D. Kralj, *Powder Technol.*, 2007, **171**, 192–199.
- 27 R. Chang, S. Kim, S. Lee, S. Choi, M. Kim and Y. Park, *Front. Energy Res.*, 2017, **5**, 17.
- 28 J. Polte, T. T. Ahner, F. Delissen, S. Sokolov, F. Emmerling, A. F. Thünemann and R. Kraehnert, *J. Am. Chem. Soc.*, 2010, **132**, 1296–1301.
- 29 K. M. Lange, A. Kothe and E. F. Aziz, *Phys. Chem. Chem. Phys.*, 2012, **14**, 5331–5338.
- 30 Y. Ohkubo, T. Nakagawa, S. Seino, J. Kugai, T. A. Yamamoto, H. Nitani and Y. Niwa, *J. Synchrotron Radiat.*, 2014, **21**, 1148–1152.
- 31 S. G. Booth, A. Uehara, S.-Y. Chang, J. F. W. Mosselmans, S. L. M. Schroeder and R. A. W. Dryfe, *J. Phys. Chem. C*, 2015, **119**, 16785–16792.
- 32 K. S. Elvira, X. C. i Solvas, R. C. R. Wootton and A. J. deMello, *Nat. Chem.*, 2013, **5**, 905–915.
- 33 A. Dey, G. de With and N. A. J. M. Sommerdijk, *Chem. Soc. Rev.*, 2010, **39**, 397–409.
- 34 Y. Chao, O. Horner, P. Vallée, F. Meneau, O. Alos-Ramos, F. Hui, M. Turmine, H. Perrot and J. Lédion, *Langmuir*, 2014, **30**, 3303–3309.
- 35 Q. Zhang, Y. Jiang, B.-D. Gou, J. Huang, Y.-X. Gao, J.-T. Zhao, L. Zheng, Y.-D. Zhao, T.-L. Zhang and K. Wang, *Cryst. Growth Des.*, 2015, **15**, 2204–2210.

